

Three discontinuous Galerkin schemes for the anisotropic heat conduction equation on non-aligned grids

M. Held,^{1, a)} M. Wiesenberger,¹ and A. Stegmeir²

¹⁾*Institute for Ion Physics and Applied Physics, University of Innsbruck, Technikerstrasse 25, A-6020 Innsbruck, Austria*

²⁾*Max-Planck-Institut für Plasmaphysik, Boltzmannstrasse 2, 85748 Garching, Germany*

We present and discuss three discontinuous Galerkin (dG) discretizations for the anisotropic heat conduction equation on non-aligned cylindrical grids. Our most favourable scheme relies on a self-adjoint local dG (LDG) discretization of the elliptic operator. It conserves the energy exactly and converges with arbitrary order. The pollution by numerical perpendicular heat fluxes degrades with superconvergence rates. We compare this scheme with aligned schemes that are based on the flux-coordinate independent approach for the discretization of parallel derivatives. Here, the dG method provides the necessary interpolation. The first aligned discretization can be used in an explicit time-integrator. However, the scheme violates conservation of energy and shows up stagnating convergence rates for very high resolutions. We overcome this partly by using the adjoint of the parallel derivative operator to construct a second self-adjoint aligned scheme. This scheme preserves energy, but reveals unphysical oscillations in the numerical tests, which result in a decreased order of convergence. Both aligned schemes exhibit low numerical heat fluxes into the perpendicular direction. We build our argumentation on various numerical experiments on all three schemes for a general axisymmetric magnetic field, which is closed by a comparison to the aligned finite difference (FD) schemes of References^{1,2}.

^{a)}Electronic mail: Markus.Held@uibk.ac.at

I. INTRODUCTION

Strong magnetic fields are known to separate the scales of turbulent motion in thermonuclear fusion or astrophysical plasmas. Along and perpendicular to magnetic field lines the mean free paths are of the order of the connection length and of the gyroradius. This introduces a strong anisotropy into the magnetized plasma, resulting in viscosity and heat conduction coefficients, which are several magnitudes higher in the parallel direction than into the perpendicular direction.

In order to formulate the problem we split the gradient into parallel and perpendicular parts via

$$\nabla =: \hat{\mathbf{b}}\nabla_{\parallel} + \nabla_{\perp}, \quad (1)$$

where $\nabla_{\parallel} = \hat{\mathbf{b}} \cdot \nabla$, and $\hat{\mathbf{b}}(\mathbf{x}) = \mathbf{B}/B$ is the unit vector in the magnetic field direction. With this definition we can split the diffusion operator into

$$\Delta f = \nabla^2 f = \nabla \cdot (\hat{\mathbf{b}}\hat{\mathbf{b}} \cdot \nabla + \nabla_{\perp})f =: \Delta_{\parallel}f + \Delta_{\perp}f. \quad (2)$$

In the following we mean to study the exemplary model of the anisotropic heat conduction equation

$$\frac{\partial}{\partial t}T = \chi_{\parallel}\Delta_{\parallel}T + \chi_{\perp}\Delta_{\perp}T, \quad (3)$$

with constant parallel and perpendicular heat conduction coefficients χ_{\parallel} and χ_{\perp} . Since in magnetized plasmas the parallel heat conduction is orders of magnitudes higher than the perpendicular heat conduction, we assume that χ_{\perp} is zero. The energy $E = \int_{\Omega} dV T$ is invariant over time if the surface integral $\int_{\partial\Omega} d\mathbf{A} \cdot \mathbf{b}\nabla_{\parallel}T = 0$ on the boundary $\partial\Omega$ of the domain Ω .

The anisotropy imposes stringent requirements on the numerical method, which is commonly solved by aligning the coordinates with the magnetic field³. However, aligned flux coordinates exhibit nonorthogonal and anisotropic meshes while not resolving singular points (e.g.: X- and O-point). Especially near the last closed flux surface of fusion plasmas those points result into severe numerical problems, which could only partly overcome by additional coordinate transformations^{4,5}. Here, the shifted metric transformation⁴ remedies the nonorthogonality and the conformal tokamak coordinates⁵ produce isotropic meshes for a

proper treatment of shaped nonsingular flux surfaces.

The contrary approach is to misalign the numerical grid to the magnetic field. Consequently one has to tackle numerical issues, which are most significantly convergence loss⁶ and numerical perpendicular heat flux that exceeds the true perpendicular heat transport⁷. Hence, proper and more sophisticated numerical discretization techniques are unavoidable. In general we can distinguish between non-aligned and aligned discretizations. The former methods have proven successful for finite differences⁷ and higher-order finite elements^{8,9} even for huge levels of anisotropy $\chi_{\parallel}/\chi_{\perp} = 10^9$. The symmetric difference scheme of⁷ is founded on the support operator method (SOM) introduced in Reference¹⁰, which is also known as Mimetic Finite Difference (MFD) method. Its main idea is to define the divergence operator as the adjoint of the gradient operator, resulting in a self-adjoint diffusion operator. This concept has also reached LDG methods, which are effectively used to solve parabolic and elliptic equations¹¹. However, so far the properties of LDG method have not been investigated for anisotropic heat conduction in magnetized fusion plasmas.

Aligned schemes rely either on 2D^{1,2,12} or 3D interpolation¹³, and fix either the toroidal angle $\Delta\varphi$ or the length of the field line Δs . The interpolation points are found by tracing the magnetic field line with an appropriate integration method. Here, less accurate schemes neglect the detailed curvature of the magnetic field line and employ an approximate aligned stencil.

The flux-coordinate independent (FCI) approach is an aligned 2D interpolation scheme, which approximates the parallel gradient ∇_{\parallel} with a central finite difference¹². In that case, high-order 2D interpolation techniques have effectively reduced numerical perpendicular diffusion. Here, a parallel advection equation supported the usability of the FCI approach even for diverted axisymmetric magnetic fields¹⁴. The FCI approach was adapted to the MFD method to tackle the anisotropic diffusion equation¹. It was shown that the self-adjoint discretization of the diffusion operator exhibits less numerical perpendicular diffusion than a naive discretization^{1,2,15}. In this paper we lay the focus on the numerical investigation of the convergence rate of the aligned finite difference schemes for magnetic fields with $\nabla \cdot \hat{\mathbf{b}} \neq 0$, which has not yet been considered.

Aligned differences with 3D interpolation can be extended to yield comparable numerical perpendicular heat fluxes to non-aligned finite differences in the case of magnetic fields with $\nabla \cdot \hat{\mathbf{b}} = 0$ ¹³. However, for $\nabla \cdot \hat{\mathbf{b}} \neq 0$ and closed field lines along the symmetry axis it was

unfolded that convergence is lost for high levels of anisotropy.

The emphasis of all the so far mentioned schemes is put on magnetized fusion plasmas where only low temperature gradients along the magnetic field are expected. An extensive discussion on monotonicity preserving schemes, which are eligible for astrophysical plasmas can be found in Reference¹⁶.

In this work we present a non-aligned scheme based on the local discontinuous Galerkin (LDG) method. This scheme is formulated in the spirit of the SOM¹⁰, so that the resulting diffusion operator is self-adjoint. This results in exact energy conservation and a vast reduction of unphysical perpendicular heat fluxes. Moreover the order of the scheme is arbitrary. However, the non-aligned discretization suffers from a restrictive Courant-Friedrichs-Lewy (CFL) condition, which is circumvented by an implicit time integrator. On the other side we implemented two aligned schemes of second order into the dG method, which were motivated from finite differences and rely on 2D interpolation^{1,12}. The first scheme is not self-adjoint and fails in conserving energy exactly. We show numerically that in contrast to the direct aligned FD scheme the convergence is lost for higher resolutions. Hence the direct aligned dG scheme is not robust for general axisymmetric magnetic fields. The second aligned scheme is also self-adjoint so that energy is conserved. This scheme is corrected due to jumps at the cell boundaries, which are accompanied by an unfavourable CFL condition and require an implicit treatment. Numerical tests reveal irregular and reduced convergence rates, which is in accordance with the results of the self-adjoint aligned FD discretization. This is owed to corrugations which occur on the grid scale. However, both aligned dG schemes demonstrate low perpendicular pollution even in cases of coarse resolutions. All our proposed schemes are tested for an axisymmetric magnetic field where the divergence of $\hat{\mathbf{b}}$ is not vanishing. The computations of the dG schemes were conducted with **FELTOR** (Full-F **E**lectromagnetic model in **TOR**oidal geometry), which exploits the high degree of parallelism on GPUs and CPUs on shared and distributed memory systems¹⁷. **GRILLIX** provides the simulations for the aligned FD schemes via an efficient hybrid parallelization for CPUs¹⁵.

II. THEORY

The theory part is split into the non-aligned and the aligned schemes. We start with the non-aligned scheme and illustrate the discretization of first derivatives with the LDG method

in Section II A 2. The adjoint of those derivatives can then be used to discretize the elliptic equation as set out in Section II B. In Section II C we present the aligned discretizations of the parallel derivative. Those make use of the Legendre polynomials for the 2D interpolation. The theory part is closed with a short description of the implemented time-discretizations in Section II D.

A. Non-aligned discretization of the parallel derivative

1. Legendre polynomials

Our discontinuous Galerkin methods are based on the use of orthogonal Legendre polynomials up to order $P - 1$. We define x_j^a and w_j , $j = 0, \dots, P - 1$ denoting the abscissas and weights of the Gauss–Legendre quadrature on the interval $[-1, 1]$ and denote $p_k(x)$ as the $k - th$ Legendre polynomial (see e.g.¹⁸). With this, we define the forward transformation matrix

$$F^{kj} := \frac{2k + 1}{2} w_j p_k(x_j^a). \quad (4)$$

Let us now consider an interval $[a, b]$ and an equidistant discretization by N cells with cell center x_n and grid size $h = \frac{b-a}{N}$; in addition, we set $x_{nj}^a := x_n + \frac{h}{2} x_j^a$. Given a function $f : [a, b] \rightarrow \mathbb{R}$ we then define $f_{nj} := f(x_{nj}^a)$ and denote its dG expansion

$$f_h(x) = \sum_{n=1}^N \sum_{k,j=0}^{P-1} F^{kj} f_{nj} p_{nk}(x). \quad (5)$$

Here, $p_{nk}(x)$ is the $k - th$ Legendre polynomial in cell n

$$p_{nk}(x) := \begin{cases} p_k\left(\frac{2}{h}(x - x_n)\right), & \text{for } x - x_n \in \left[-\frac{h}{2}, \frac{h}{2}\right] \\ 0, & \text{else.} \end{cases} \quad (6)$$

Let us define the diagonal weights matrix W and its inverse V

$$W^{ij} := \frac{h w_j}{2} \delta_{ij}, \quad (7a)$$

$$V_{ij} := W_{ij}^{-1} = \frac{2}{h w_j} \delta_{ij}. \quad (7b)$$

The use of Legendre polynomials yields a natural approximation of the L^2 scalar product via Gauss–Legendre quadrature

$$\langle f_h, g_h \rangle := \int_a^b f_h g_h \, dx = \sum_{n=1}^N \sum_{j=0}^{P-1} \frac{hw_j}{2} f_{nj} g_{nj} = \mathbf{f}^T (\mathbf{1} \otimes W) \mathbf{g}, \quad (8a)$$

$$\|f_h\|_{L^2}^2 := \int_a^b |f_h|^2 \, dx = \sum_{n=1}^N \sum_{j=0}^{P-1} \frac{hw_j}{2} f_{nj}^2 = \mathbf{f}^T (\mathbf{1} \otimes W) \mathbf{f}, \quad (8b)$$

where \otimes denotes the Kronecker product. With these formulas we have a simple, accurate, and fast method to evaluate integrals. This is applied, for example, to compute errors in the L^2 -norm. Function products are easily computed pointwise, i.e.

$$(f_h g_h)_{ni} = f_{ni} g_{ni}. \quad (9)$$

2. The first derivatives

The derivative of $p_{ni}(x)$ is not well defined on cell boundaries, which is why we now retain to a weak formulation. Consider

$$\int_{C_n} \partial_x f_h(x) p_{ni}(x) \, dx = f_h p_{ni} \Big|_{x_{n-1/2}}^{x_{n+1/2}} - \int_{C_n} f_h(x) \partial_x p_{ni}(x) \, dx. \quad (10)$$

The approximation $f_h(x)$ is double valued on the cell boundaries. The boundary terms have to be replaced by

$$\int_{C_n} f_x p_{ni}(x) \, dx = \hat{f} p_{ni} \Big|_{x_{n-1/2}}^{x_{n+1/2}} - \int_{C_n} \bar{f}^{nk} p_{nk} \partial_x p_{ni} \, dx, \quad (11)$$

where $\hat{f}(x)$ is the numerical flux across cell boundaries and we call $f_x(x)$ the numerical approximation to the first derivative. Let us define

$$f^+(x) := \lim_{\varepsilon \rightarrow 0, \varepsilon > 0} f_h(x + \varepsilon), \quad (12a)$$

$$f^-(x) := \lim_{\varepsilon \rightarrow 0, \varepsilon > 0} f_h(x - \varepsilon). \quad (12b)$$

We construct the numerical flux by the mean value $\{\{f\}\} := (f^+ + f^-)/2$ and the jumps $[[f]] := (f^+ - f^-)/2$ at the cell boundaries

$$\hat{f} = \{\{f\}\} + C [[f]] \quad (13)$$

with $C := \{0, 1, -1\}$ determining the centered(C), forward(F) and the backward(B) flux respectively¹⁹. For $f: [a, b] \rightarrow \mathbb{R}$ we assume that

$$f(b + \varepsilon) = f(a + \varepsilon), \quad f(a - \varepsilon) = f(b - \varepsilon), \quad (14a)$$

$$\hat{f}(a) = \hat{f}(b) = 0, \quad (14b)$$

$$\hat{f}(a) = f^+(a), \quad \hat{f}(b) = f^-(b). \quad (14c)$$

for periodic, homogeneous Dirichlet and homogeneous Neumann boundary conditions respectively. Depending on what flux we choose, we arrive at various approximations to the derivative, e.g. for $P = 1$ (i.e. a piecewise constant approximation in each cell) our scheme reduces to the classic centered, forward and backward finite difference schemes respectively.

The derivative can be written as a matrix-vector multiplication

$$\mathbf{f}_x = D_x \mathbf{f}. \quad (15)$$

For a concise notation we define

$$D_x := (\mathbf{1} \otimes V) \cdot (\mathbf{1} \otimes F^T) \cdot \bar{D}_x \cdot (\mathbf{1} \otimes F).$$

We now show the matrix representation of the centered, forward, and backward one-dimensional discrete derivative for periodic boundary conditions that can be used in the implementation

$$\bar{D}_{x,per}^0 = \frac{1}{2} \begin{pmatrix} (M - M^T) & RL & & -LR \\ -LR & (M - M^T) & RL & \\ & -LR & \dots & \\ & & \dots & RL \\ RL & & -LR & (M - M^T) \end{pmatrix}, \quad (16)$$

$$\bar{D}_{x,per}^+ = \begin{pmatrix} -(M + LL)^T & RL & & 0 \\ 0 & -(M + LL)^T & RL & \\ & 0 & \dots & \\ & & \dots & RL \\ RL & & 0 & -(M + LL)^T \end{pmatrix}, \quad (17)$$

and

$$\bar{D}_{x,per}^- = \begin{pmatrix} (M + LL) & 0 & & -LR \\ -LR & (M + LL) & 0 & \\ & -LR & \dots & \\ & & & \dots & 0 \\ 0 & & & -LR & (M + LL) \end{pmatrix}. \quad (18)$$

We used the notation

$$RR_{ij} := 1 = RR_{ij}^T, \quad RL_{ij} := (-1)^j, \quad (19a)$$

$$LL_{ij} := (-1)^{i+j} = LL_{ij}^T, \quad LR_{ij} := (-1)^i = RL_{ij}^T, \quad (19b)$$

$$M_{ij} := \begin{cases} 0, & \text{for } i > j - 1 \\ 1 - (-1)^{i+j} & \text{else} \end{cases}, \quad (19c)$$

which we introduce mainly for ease of implementation. If a block-matrix class is written and the operations $+$, $-$ and $*$ are defined on it, the assembly of the derivative matrices is simplified to a large extent. Note that for $P = 1$ we recover the familiar finite difference approximations of the first derivative. Finally, we note the boundary terms for homogeneous

TABLE I: Upper left and lower right matrix entries for various boundary conditions. For Dirichlet and von Neumann BC the upper right and lower left entries are zero.

	D_x^+ (forward)		D_x^- (backward)		D_x^0 (centered)	
	left	right	left	right	left	right
periodic	$-(M + L)^T$	$-(M + L)^T$	$(M + L)$	$(M + L)$	$\frac{1}{2}(M - M^T)$	$\frac{1}{2}(M - M^T)$
Dirichlet	$-M^T$	$-(M + L)^T$	$(M + L)$	$-M^T$	$\frac{1}{2}(M - M^T + L)$	$\frac{1}{2}(M - M^T - R)$
Neumann	$-(M + L)^T$	M	M	$(M + L)$	$\frac{1}{2}(M - M^T - L)$	$\frac{1}{2}(M - M^T + R)$

Dirichlet and Neumann boundaries in Table (I) noticing that only the corner entries of the matrices change.

The generalization to higher dimensions is immediate. All the matrices derived above can readily be extended via the appropriate Kronecker products. The space complexity of the matrices derived is $\mathcal{O}(P^2N)$ in one, $\mathcal{O}(P^3N^2)$ in two and $\mathcal{O}(P^4N^3)$ in three dimensions. We do so for the parallel derivative, which can be written as $\nabla_{\parallel} = b^R \partial_R + b^Z \partial_Z + b^\varphi \partial_\varphi$. The

discrete centered, forward and backward derivatives are

$$G_0 = b^R \circ D_R^0 + b^Z \circ D_Z^0 + b^\varphi \circ D_\varphi^0, \quad (20)$$

$$G_+ = b^R \circ D_R^+ + b^Z \circ D_Z^+ + b^\varphi \circ D_\varphi^+, \quad (21)$$

$$G_- = b^R \circ D_R^- + b^Z \circ D_Z^- + b^\varphi \circ D_\varphi^-, \quad (22)$$

where \circ denotes pointwise multiplication.

3. The adjoint of a matrix

Recall that the adjoint of a matrix A is defined by the scalar product, i.e.

$$\mathbf{f}^T \cdot [(\mathbf{1} \otimes W) \cdot A] \cdot \mathbf{g} = \mathbf{g}^T \cdot [A^T \cdot (\mathbf{1} \otimes W)] \cdot \mathbf{f} =: \mathbf{g}^T \cdot [(\mathbf{1} \otimes W)A^\dagger] \cdot \mathbf{f}.$$

From here we immediately get the relation

$$A^\dagger \equiv (\mathbf{1} \otimes V) \cdot A^T \cdot (\mathbf{1} \otimes W). \quad (23)$$

There is a close connection between symmetric, $A = A^T$, and self-adjoint, $A = A^\dagger$, matrices. If and only if the matrix A is symmetric, then $(\mathbf{1} \otimes V) \cdot A$ is self-adjoint. Of course, we have $(A \cdot B)^\dagger = B^\dagger \cdot A^\dagger$ and $(A^\dagger)^\dagger = A$. Since the volume form in cylindrical coordinates reads $RdRdZd\varphi$ we have to multiply the weights by R when computing the adjoint of matrices in this case.

B. Discretization of elliptic equations

First, we discretize the one-dimensional general elliptic equation

$$-\frac{\partial}{\partial x} \left(\chi(x) \frac{\partial f(x)}{\partial x} \right) = \rho(x) \quad (24)$$

on the interval $[a, b]$ and define the flux $q := \chi(x) \frac{\partial f(x)}{\partial x}$. Here, $\chi(x)$ and $\rho(x)$ are given functions.

We either choose periodic, Dirichlet, or Neumann boundary conditions on the left and right border for f . Our plan is to simply use one of the discretizations developed in the last section for the right derivative and its adjoint for the left derivative. The multiplication with χ is a simple function product

$$D_x^\dagger \cdot \chi \cdot D_x \mathbf{f} = \rho, \quad (25)$$

where D_x is either D_x^+ , D_x^- , or D_x^0 with the correct boundary terms and D_x^\dagger is its adjoint according to Eq. (23). Note, that¹⁹ originally only proposed to use the forward or backward discretization for D_x . Eq. (25) is indeed a self-adjoint discretization for the second derivative. However, it turns out that Eq. (25) is inconsistent for given $\rho(x)$. The solution does not converge for $P > 1$. This problem is solved according to¹⁹ by adding a jump term $[[f]]$ to the numerical flux of q in the case $P > 1$

$$\hat{q} = \{\{q\}\} + C [[q]] - [[f]]. \quad (26)$$

That means we have to alter our discretization (25) according to

$$[D_x^\dagger \cdot \chi \cdot D_x + J] \mathbf{f} = \rho, \quad (27)$$

where again $J = (\mathbf{1} \otimes V)(\mathbf{1} \otimes F^T)\bar{J}(\mathbf{1} \otimes F)$ and

$$\bar{J} = \begin{pmatrix} (LL + RR) & -RL & & -LR \\ -LR & (LL + RR) & -RL & \\ & -LR & \dots & \\ & & & \dots & -RL \\ -RL & & & -LR & (LL + RR) \end{pmatrix} \quad (28)$$

for periodic boundaries. Again we give the correct boundary terms for Dirichlet and Neumann boundary conditions in Table II. Note that \bar{J} is symmetric, thus the overall dis-

	J	
	left	right
periodic	$L + R$	$L + R$
Dirichlet	$L + R$	$L + R$
Neumann	R	L

TABLE II: Top left and bottom right entries for jump matrix

cretization remains self-adjoint. Indeed, with $D_x = D_x^+$ Eq. (27) recovers the discretization proposed by¹⁹. In addition, we remark that the centered discretization in Eq. (27) is symmetric with respect to an inversion of the coordinate system $x \rightarrow -x$ even for double Dirichlet or Neumann boundaries, while the forward and backward discretization is not.

C. Aligned discretization of the parallel derivative

We begin with the formulation of a field-aligned discretization. If s denotes the field line following coordinate, then the one-dimensional discrete derivative along the field line reads

$$\frac{df}{ds} \rightarrow \frac{f_{k+1} - f_{k-1}}{s_{k+1} - s_{k-1}}. \quad (29)$$

From differential geometry we know that to every smooth vector field $\hat{\mathbf{b}}$ there is a unique curve of which the tangent in a point is the value of $\hat{\mathbf{b}}$ at that point²⁰. It is given by the solution of the differential equation

$$\frac{dz^i}{ds} = \hat{b}^i(\mathbf{z}), \quad (30)$$

where z^i is one of (R, Z, φ) and \hat{b}^i are the contravariant components of $\hat{\mathbf{b}}$ in cylindrical coordinates. Moreover, by definition we have

$$\frac{df(\mathbf{z}(s))}{ds} = \hat{\mathbf{b}} \cdot \nabla f|_{\mathbf{z}(s)} \quad (31)$$

along a field line parameterized by distance s , i.e. instead of $\nabla_{\parallel} f$ we can choose to discretize $\frac{df}{ds}$.

Let us divide the φ direction into N_{φ} equidistant planes of distance $\Delta\varphi$. Unfortunately, from Eq. (30) we cannot easily determine the distance Δs for given $\Delta\varphi$. It is better to integrate

$$\frac{dz^i}{dt} = \frac{b^i}{b^{\varphi}} = \frac{B^i}{B^{\varphi}} \quad (32)$$

since in this case $d\varphi/dt = 1 \Rightarrow t = \varphi$. We get

$$\frac{dR}{d\varphi} = \frac{B^R}{B^{\varphi}}, \quad (33a)$$

$$\frac{dZ}{d\varphi} = \frac{B^Z}{B^{\varphi}}, \quad (33b)$$

together with the equation

$$\frac{ds}{d\varphi} = \frac{1}{|\hat{b}^{\varphi}|} = \frac{B}{|B^{\varphi}|} \quad (33c)$$

for the length of the field line s . Eqs. (33) are integrated from $\varphi = 0$ to $\varphi = \pm\Delta\varphi$. We characterize the flow generated by $\hat{\mathbf{b}}/b^{\varphi}$ by

$$T_{\Delta\varphi}^{\pm 1} \mathbf{z} := T_{\Delta\varphi}^{\pm 1}[R, Z, \varphi] := (R(\pm\Delta\varphi), Z(\pm\Delta\varphi), \varphi \pm \Delta\varphi), \quad (34)$$

where $(R(\varphi), Z(\varphi), s(\varphi))$ is the solution to Eqs. (33) with initial condition

$$(R(0), Z(0), s(0)) = (R, Z, 0). \quad (35)$$

Obviously we have $T_{\Delta\varphi}^{-1} \cdot T_{\Delta\varphi}^{+1} = \mathbf{1}$, but $T_{\Delta\varphi}^{\pm}$ is not unitary since $\hat{\mathbf{b}}/b^\varphi$ is not divergence free.

The proposed centered discretization (29) for the parallel derivative then reads

$$\nabla_{\parallel} f \equiv \frac{df}{ds} = \frac{df}{d\varphi} \frac{d\varphi}{ds} \rightarrow \frac{f(T_{\Delta\varphi}^+ \mathbf{z}) - f(T_{\Delta\varphi}^- \mathbf{z})}{s(+\Delta\varphi) - s(-\Delta\varphi)}, \quad (36)$$

which is slightly different from Reference¹⁴, where the relation (33c) was used to replace $d\varphi/ds$. Previous derivations now needed to construct an interpolation scheme in order to evaluate functions on the transformed coordinates. Since the R and Z coordinates are discretized in the dG framework we note that in our work the interpolation of f on the transformed points $T_{\Delta\varphi}^{\pm 1} \mathbf{z}$ is naturally given by Eq. (5) (the extension to two dimensions is immediate). Let us for a moment omit the Z coordinate for ease of notation. If (R_{nj}, φ_k) are the grid points, we call $(R_{nj}^+, \varphi_{k+1}) := T_{\Delta\varphi}^+[R_{nj}, \varphi_k]$ and $(R_{nj}^-, \varphi_{k-1}) := T_{\Delta\varphi}^-[R_{nj}, \varphi_k]$ the transformed coordinates along the field lines. We then have

$$f(T_{\Delta\varphi}^+ \mathbf{z}) = f(R_{nj}^+, \varphi_{k+1}) = \bar{f}_{k+1}^{ml} p_{ml}(R_{nj}^+) =: (I^+)_{knj}^{qml} f_{qml}, \quad (37a)$$

$$f(T_{\Delta\varphi}^- \mathbf{z}) = f(R_{nj}^-, \varphi_{k-1}) = \bar{f}_{k-1}^{ml} p_{ml}(R_{nj}^-) =: (I^-)_{knj}^{qml} f_{qml}, \quad (37b)$$

where the backward transformations $\bar{\mathbf{f}} := (\mathbf{1} \otimes F)\mathbf{f}$ are hidden in I . Thus, the interpolation of all the necessary points can simply be written as a matrix-vector product, where the interpolation matrices I^+ and I^- are independent of time since the magnetic field is assumed constant in time. The order of this interpolation is given by P , the number of polynomial coefficients. A consistency check is the relation $I^+ \cdot I^- = \mathbf{1}$.

The centered discretization (36) can now be written as a matrix vector product according to

$$Q_0 f = S_0 \cdot [I^+ - I^-] f, \quad (38)$$

where S_0 is the diagonal matrix that contains the entries $(s(+\Delta\varphi) - s(-\Delta\varphi))^{-1}$. This discretization is not skew-symmetric since the field lines are not volume-preserving, or $(I^+)^T \neq I^-$. The forward (+) and backward (-) operators Q for the parallel derivative are formulated analogously to

$$Q_+ f = S_+ \cdot [I^+ - I] f, \quad (39a)$$

$$Q_- f = S_- \cdot [I^- - I] f, \quad (39b)$$

where S_{\pm} is the diagonal matrix that contains the entries $(s(\pm\Delta\varphi))^{-1}$.

1. *Boundary conditions*

The main problem with the above scheme is the question what to do when a field line crosses the simulation boundaries. Boundary conditions(BC) are formulated in cylindrical coordinates and are either homogeneous Dirichlet or Neumann. The latter are straightforward and implemented by setting $\nabla_{\parallel}f = 0$ if the field line leaves the computational domain. For Dirichlet BCs one idea is to simply cut the contribution from field lines that leave the computational domain. While this works in practice it is unclear what numerical and physical side-effects this procedure might have. Another idea is to check to every point \mathbf{z} whether $T_{\Delta\varphi}\mathbf{z}$ lies inside our simulation box or not. If not, we have to find where exactly the field line intersects the simulation box. We have to find φ_b such that the result of the integration of Eq. (33) from 0 to φ_b lies on the boundary. The angle φ_b can be found by a bisection algorithm knowing that $0 < \varphi_b < \Delta\varphi$. This kind of procedure is known as a shooting method. When all points are found, ghost cells can be constructed in the correct way.

D. **Time-stepping**

Having discretized the spatial derivatives of Eq. (3), we can now independently choose a discretization in time. This is known as the method of lines. In order to be able to test both explicit and implicit methods we implemented a semi-implicit Runge-Kutta (SIRK) scheme²¹. The scheme is of third order in the explicit terms and of second order in the implicit terms. The method combines the cost-effectiveness of explicit algorithms with the stability of purely implicit time-steppers. We solve the implicit substeps by a conjugate gradient method, which works as long as the implicit part remains symmetric and linear. We finally remark that, given the explicit and implicit parts, an implementation of the time-stepper only require linear algebra vector space operations. In fact, all of the up to now discussed algorithms can be implemented using basic vector-vector operations and a sparse matrix-vector product.

III. THREE DG SCHEMES

We are now ready to propose three different numerical approximations D to the parallel Diffusion operator Δ_{\parallel} .

A. Direct aligned dG discretization

In the first approximation we apply the divergence free property of the magnetic field \mathbf{B} and write $\nabla \cdot (\hat{\mathbf{b}}f) = B\nabla_{\parallel}(B^{-1}f)$. We then use one of the centered, forward or backward aligned discretizations of the parallel derivative of Section II C to get a discretization of $\Delta_{\parallel}f = B\nabla_{\parallel}(B^{-1}\nabla_{\parallel}f)$. Hence, we can formulate two schemes based on either centered differences or an arithmetic average over the forward and backward differences

$$D_0^D f = BQ_0B^{-1}Q_0f, \quad D_a^D f = \frac{1}{2} [BQ_+B^{-1}Q_+f + BQ_-B^{-1}Q_-f]. \quad (40)$$

In contrast to the naive discretization of Reference¹, this scheme holds for magnetic fields with $\nabla \cdot \mathbf{b} \neq 0$ and makes use of the Legendre polynomials for the interpolation.

B. Self-adjoint aligned dG discretization

We note the adjoint of the parallel derivative:

$$\nabla_{\parallel}^{\dagger} f = -\nabla \cdot (\hat{\mathbf{b}} f). \quad (41)$$

With this relation we can define the parallel diffusion operator of Eq. (2) to be self-adjoint according to

$$\Delta_{\parallel} = -\nabla_{\parallel}^{\dagger} \nabla_{\parallel}. \quad (42)$$

This leads to the idea to simply use a discretization for the parallel derivative and use the matrix adjoint Eq. (23) to get a discretization for the divergence. Hence, we can derive the self-adjoint discretization for centered and averaged differences

$$D_0^A f = [Q_0^{\dagger}Q_0 + J] f, \quad D_a^A f = \frac{1}{2} [Q_+^{\dagger}Q_+ + Q_-^{\dagger}Q_- + 2J] f. \quad (43)$$

The scheme is similar to that of Reference¹ except for the interpolation technique, and that in the dG framework we have to add the jump term J of Eq. (27) to obtain a convergent and stable diffusion operator.

C. Self-adjoint non-aligned LDG discretization

The directional derivative $\nabla_{\parallel} = \hat{\mathbf{b}} \cdot \nabla$ can be discretized directly as $\nabla_{\parallel} = b^R \partial_R + b^Z \partial_Z + b^{\varphi} \partial_{\varphi}$ using the dG methods developed in the Section II A 2. The adjoint of the resulting matrix is then a discretization for the divergence $\nabla \cdot (\hat{\mathbf{b}} f)$ again. The composition of both yields then a discretization for the parallel Laplacian according to

$$D_0^G f = \left[G_0^\dagger G_0 + J \right] f, \quad D_a^G f = \frac{1}{2} \left[G_+^\dagger G_+ + G_-^\dagger G_- + 2J \right] f. \quad (44)$$

Note, that we add jump terms for stabilization once more.

IV. TWO ALIGNED FD SCHEMES

The dG schemes are compared to two aligned FD discretizations, presented in References^{1,2,15}. The first aligned FD scheme is a generalization of the naive scheme, which is based on third order bipolynomial interpolation (**N-3**) and was originally proposed to discretize ∇_{\parallel}^2 . The operator $(\nabla \cdot \hat{\mathbf{b}}) \nabla_{\parallel}$ was added to this scheme so that effects arising from $\nabla \cdot \hat{\mathbf{b}} \neq 0$ are taken into account. The discrete parallel gradient is thereby computed via a central finite difference along magnetic field lines¹², and the resultant scheme is denominated **D-3**. The second aligned FD schemes **S-3** is formulated in the spirit of the SOM. In the **S-3** scheme the discrete parallel gradient is also computed with the help of third order bipolynomial interpolation. The parallel diffusion operator then follows via requiring its self-adjointness property on the discrete level.

V. TESTS

We use an axisymmetric magnetic field with $\nabla \cdot \hat{\mathbf{b}} \neq 0$. In cylindrical coordinates $\{R, Z, \varphi\}$ it is given by

$$\mathbf{B} = I_0 \nabla \varphi + \nabla \psi_p \times \nabla \varphi, \quad (45)$$

with $I_0 = 20$, $R_0 = 10$ and a poloidal flux of the form

$$\psi_p = \cos\left(\frac{\pi}{2}(R - R_0)\right) \cos\left(\frac{\pi}{2}Z\right). \quad (46)$$

We perform all our numerical tests on the domain $R \in [9, 11]$, $Z \in [-1, 1]$ and $\varphi \in [0, 2\pi]$. With this choice of parameters the magnetic field never crosses the simulation box.

A. Convergence test to an analytical test function

First, we define a general test function $f = -\psi_p(R, Z) \cos(\varphi)$, which fulfills Dirichlet as well as Neumann boundary conditions. We use this function to directly compute the relative error $\epsilon_{\Delta_{\parallel}f} = \|Df - \Delta_{\parallel}f\|_{L^2} / \|\Delta_{\parallel}f\|_{L^2}$ between the numerical diffusion operator Df and the analytical solution $\Delta_{\parallel}f$. At this point we introduce also a second relative error $\epsilon_f = \|f_D - f\|_{L^2} / \|f\|_{L^2}$, which is computed by inverting the diffusion operator with a conjugate gradient method. On the continuous level this would result in an ill-posed problem. However, the discrete parallel diffusion operator contains always a small amount of numerical perpendicular diffusion, which makes the discrete operator invertible.

All the so far mentioned aligned schemes are constructed to converge with order two in $\Delta\varphi$ for a homogeneous magnetic field². Moreover, the order of the non-aligned scheme is arbitrary. We define this as the optimal order. For inhomogeneous magnetic fields we can observe this optimal order only if we increase the resolution in N_R , N_Z and N_φ with the correct factors, which depend on the interpolation order and the order in φ -direction. Our tested schemes are limited to interpolating polynomials of order three in $\{R, Z\}$ and of order two in φ . For the non-aligned LDG we additionally investigate the convergence rates for interpolating polynomials of order three in $\{R, Z, \varphi\}$.

1. dG schemes

In Figure 1a) we investigate the relative error for a fixed perpendicular resolution of $P_{RZ} = 3$, $N_R = N_Z = 20$ with varying resolution in φ according to $N_\varphi = \{5, 10, 20, 40, 80, 160\}$. This results in two major issues. First of all we do not see the optimal rate of convergence for all three dG schemes. In general one ends up with convergence loss for all the schemes if only the resolution in φ is raised. This is disappearing with increasing perpendicular resolution or if the anisotropy decreases. Secondly for the self-adjoint schemes the supraconvergence phenomenon of the LDG method for elliptic problems may lead to the erroneous conclusion that the schemes are non-convergent or do not converge with the optimal order. Hence we compute a different relative error ϵ_f for these schemes to show the convergence of the proposed diffusion operators¹⁹.

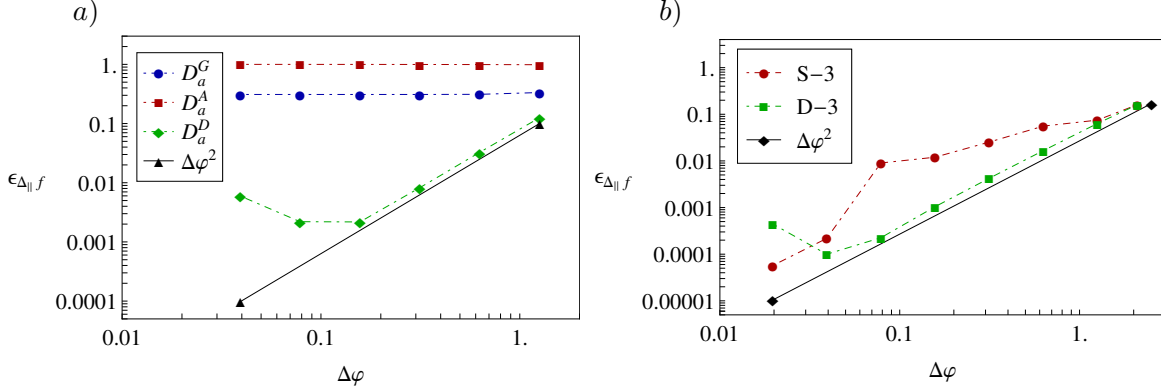


FIG. 1: a) The relative error $\epsilon_{\Delta_{\parallel}f}$ is plotted over $\Delta\varphi$ for the non-aligned LDG scheme (blue circles), the direct aligned scheme (green rhombi) and the self-adjoint aligned scheme (red squares). Here, the perpendicular resolution is fixed, which results in convergence loss for higher resolutions in φ direction. For the self-adjoint schemes the supraconvergence phenomenon of the LDG method occurs. b) The relative error $\epsilon_{\Delta_{\parallel}f}$ for the **D-3** scheme (green squared) and the **S-3** scheme (red circles) is plotted over $\Delta\varphi$ for a fixed resolution in $\{R, Z\}$.

We are now ready to show the orders of convergence of the centered and averaged discretizations. For this purpose we increase the resolutions in all directions with the correct order according to $P_{RZ} = 3$, $N_R = N_Z = 5 (2^{i2/3})$, $N_\varphi = 5 (2^i)$ with $i = \{0, 1, \dots, 5\}$. The relative errors and orders of convergence are depicted in Table III for the centered schemes and Table IV for the averaged schemes. Those tables reveal that the non-aligned LDG discretization is the only scheme, which has the optimal order of convergence for $P_\varphi = 1$ and also superconvergent rates for $P_\varphi = 3$. The aligned schemes do both show up stagnating convergence rates for higher resolutions whereas the self-adjoint aligned scheme additionally fails in converging with the optimal order of two. Instead it converges with a reduced and irregular order, casting it into a true supraconvergent discretization. This is a consequence of oscillatory relative error fields, which are shown in Figure 2 and discussed throughout the next sections. Furthermore, we note that we observed stagnating convergence rates also for the relative error of the parallel gradient operator $Q_{\{0,+,-\}}$.

TABLE III: L^2 error and orders of accuracy for the centered non-aligned LDG scheme, the centered direct aligned scheme and the centered self-adjoint aligned scheme. The L^2 error for the self-adjoint schemes is computed with ϵ_f and for the direct aligned scheme with $\epsilon_{\Delta_{\parallel}f}$

	$P_\varphi = 1$							$P_\varphi = 3$		
	D_0^G		D_0^D		D_0^A			D_0^G		
$\Delta\varphi$	L^2 error	order	L^2 error	order	L^2 error	order	$\Delta\varphi$	L^2 error	order	
$2\pi/3$	4.85E+00	–	8.29E-01	–	6.65E+00	–	$2\pi/3$	3.88E-02	–	
$2\pi/5$	7.46E-01	3.66	4.28E-01	1.30	1.11E+00	3.51	$2\pi/5$	7.58E-03	3.20	
$2\pi/10$	1.43E-01	2.39	1.25E-01	1.77	3.39E-01	1.71	$2\pi/10$	7.95E-04	3.25	
$2\pi/20$	3.36E-02	2.09	3.26E-02	1.94	1.92E-01	0.82	$2\pi/20$	6.77E-05	3.55	
$2\pi/40$	8.27E-03	2.02	8.24E-03	1.98	1.25E-01	0.62	$2\pi/30$	1.61E-05	3.55	
$2\pi/80$	2.08E-03	1.99	2.09E-03	1.98	4.50E-02	1.48	–	–	–	
$2\pi/160$	5.14E-04	2.02	5.94E-04	1.82	6.00E-02	-0.42	–	–	–	

2. Aligned FD schemes

Additionally the same convergence test was performed with the **GRILLIX** code, which is based on the aligned FD schemes depicted in Section IV. In Figure 1b) the relative error $\epsilon_{\Delta_{\parallel}f}$ for a fixed perpendicular resolution of $N_R = N_Z = 60$, ($h = 2/60$) with varying resolution in φ is shown. The **D-3** scheme behaves similar towards the D_a^D scheme, i.e. at low toroidal resolutions the convergence is of order two, but decreases at higher toroidal resolutions due to numerical perpendicular heat flux. For the **S-3** scheme the appearance of corrugations (see e.g. Figure 2) reduces if only the resolution in φ is increased. Note the strong drop of the relative error for the **S-3** scheme from $N_\varphi = 80$ to $N_\varphi = 160$, which comes along with a vast reduction of the spurious corrugations. Finally, the relative error of the **S-3** scheme is low due to the immanent small amount of numerical perpendicular heat transport.

In Table V the relative error $\epsilon_{\Delta_{\parallel}f}$ and convergence rates for the aligned FD schemes are shown. We adapted the resolution according to roughly $N_R = N_Z = 3 \cdot 5(2^{i/3})$, $N_\varphi = 5(2^i)$, $i = \{0, 1, \dots, 6\}$, where the additional factor of 3 at N_R, N_Z shall compensate for the factor $P_{RZ} = 3$ used in the test of Section V A 1. The derived relative error for the **D-3**

TABLE IV: L^2 error and orders of accuracy for the averaged non-aligned LDG scheme, the averaged direct aligned scheme and the averaged aligned self-adjoint scheme. The L^2 error for the self-adjoint schemes is computed with ϵ_f and for the direct aligned scheme with $\epsilon_{\Delta\parallel f}$

	$P_\varphi = 1$						$P_\varphi = 3$		
	D_a^G		D_a^D		D_a^A			D_a^G	
$\Delta\varphi$	L^2 error	order	L^2 error	order	L^2 error	order	$\Delta\varphi$	L^2 error	order
$2\pi/3$	4.62E-01	–	3.17E-01	–	7.77E-01	–	$2\pi/3$	3.95E-02	–
$2\pi/5$	1.43E-01	2.30	1.25E-01	1.82	2.13E-01	2.53	$2\pi/5$	7.96E-03	3.14
$2\pi/10$	3.36E-02	2.09	3.26E-02	1.94	6.66E-02	1.68	$2\pi/10$	8.46E-04	3.23
$2\pi/20$	8.27E-03	2.02	8.24E-03	1.98	4.43E-02	0.59	$2\pi/20$	8.94E-05	3.24
$2\pi/40$	2.06E-03	2.01	2.17E-03	1.92	2.42E-02	0.87	$2\pi/30$	2.42E-05	3.22
$2\pi/80$	5.15E-04	2.00	7.69E-04	1.50	2.29E-02	0.08	–	–	–
$2\pi/160$	1.29E-04	2.00	5.05E-04	0.61	4.46E-02	-0.96	–	–	–

scheme is of order two. However, similar to the D_a^D scheme it does not conserve the self-adjointness property of the parallel diffusion operator and therefore does not conserve the L^1 norm, i.e. energy (see also Section VB1). The **S-3** scheme exhibits an irregular and slower convergence behaviour. This is owed to corrugations (see Figure 2), which occur if the transformed coordinates $\mathbf{T}_{\Delta\varphi}^\pm [R_i, Z_j, \varphi_k]$ of two neighbouring grid points are in the same grid cell, respectively jump across grid cells. The mechanism is described in more detail in Reference². Apart from these corrugations the error is of the same level as for the **D-3** scheme. In general, also for magnetic fields with $\nabla \cdot \hat{\mathbf{b}} = 0$ corrugations can occur and have been observed, but they are more pronounced in situations with $\nabla \cdot \hat{\mathbf{b}} \neq 0$. As long as the corrugations remain on the grid scale (a suitable criterion for this is given in Reference²) they could possibly be cured by adding a small amount of perpendicular diffusion, which is usually anyway present in turbulence simulations.

TABLE V: Relative error $\epsilon_{\Delta_{\parallel}f}$ and its order for the aligned FD schemes.

$\Delta\varphi$	$N_{R,Z}(h)$	D-3		S-3	
		L^2 error	order	L^2 error	order
$2\pi/3$	20 (1.00E-01)	1.53E-01	—	1.53E-01	—
$2\pi/5$	20 (1.00E-01)	6.07E-02	1.81	7.15E-02	1.49
$2\pi/10$	24 (8.33E-02)	1.64E-02	1.89	5.82E-02	0.30
$2\pi/20$	40 (5.00E-02)	2.56E-03	2.00	2.22E-02	1.39
$2\pi/40$	60 (3.33E-02)	1.06E-03	1.95	1.25E-02	0.83
$2\pi/80$	100 (2.00E-02)	2.56E-04	2.04	8.30E-03	0.59
$2\pi/160$	150 (1.33E-02)	6.23E-05	2.04	6.26E-03	0.41
$2\pi/320$	240 (8.33E-03)	1.41E-05	2.14	4.70E-03	0.41

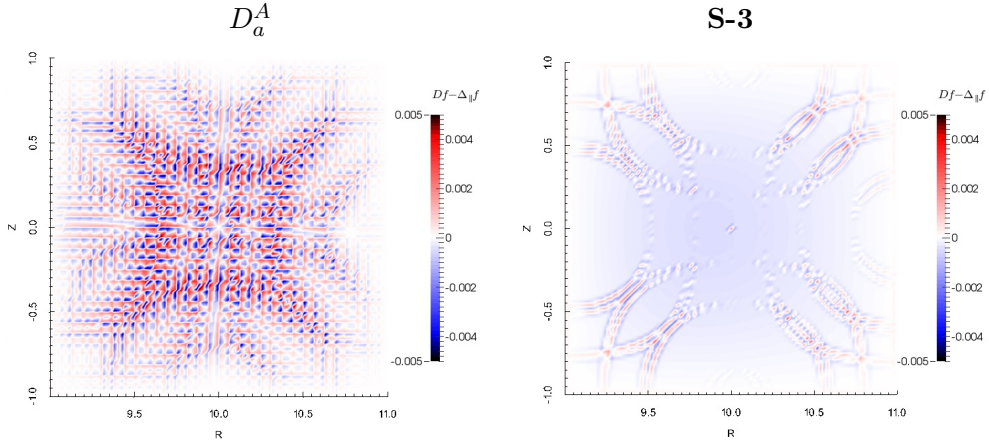


FIG. 2: The error fields $Df - \Delta_{\parallel}f$ of the convergence test are shown for the self-adjoint aligned dG scheme D_a^A and the self-adjoint aligned FD scheme **S-3** at $\varphi = 0$. The

resolution is $P_\varphi = 1$, $P_{RZ} = 3$, $N_\varphi = 80$, $N_R = N_Z = 32$ and equally $N_\varphi = 80, N_R = N_Z = 100$ for the latter. In contrast to the **S-3** scheme the oscillations/corrugations are more pronounced for the D_a^A scheme.

B. Numerical simulations

We investigate now the conservation properties and the convergence behavior of our presented schemes in numerical simulations of Eq. (3). Concerning this we use Neumann

boundary conditions to show explicitly the proposed energy conservation of our self-adjoint schemes. The convergence is examined for a general non-aligned three dimensional Gaussian blob in Section VB1. The maintenance of the most basic $k_{\parallel} = 0$ mode is shown for all schemes in Section VB. We take $\chi_{\parallel} = 100$ and $\chi_{\perp} = 0$ for all of our simulations. The time integration was either performed with a second-order implicit or third-order explicit Runge-Kutta scheme. The time step was fixed to $\Delta t = 0.001$ so that the time error can be ignored. The convergence test was performed with an even smaller timestep.

1. *Gaussian Blob*

We initialize a non-aligned Gaussian blob in φ direction of the form

$$f_0 = A \exp \left(-\frac{(R - R_b)^2}{2\sigma_R^2} - \frac{(Z - Z_b)^2}{2\sigma_Z^2} - \frac{(\varphi - \varphi_b)^2}{2\sigma_{\varphi}^2} \right) \quad (47)$$

with $A = 0.1$, $R_b = 10.6$, $Z_b = 0.0$, $\varphi_b = \pi$, $\sigma_R = \sigma_Z = 0.1$, and $\sigma_{\varphi} = 0.5$. To show the convergence of our schemes in time simulations for a general three dimensional perturbation, we perform a short highly accurate simulation over 100 time steps to $t = 0.01$ with the non-aligned LDG scheme for a resolution of $P_{RZ} = 3$, $N_R = N_Z = 51$, $P_{\varphi} = 1$ and $N_{\varphi} = 162$. This numerical reference state f_1 is used for the computation of the relative error $\epsilon_{f_1} = \|f_t - f_1\|_{L^2} / \|f_1\|_{L^2}$ at $t = 0.01$. The orders of convergence are listed in Table VI. The high perpendicular resolution should lead to convergence rates of order two if only the resolution in φ is incremented. We obtain second order convergence for the non-aligned LDG scheme and also for the direct aligned discretization. However, the self-adjoint aligned discretization has again reduced orders of convergence. This is contributed to the oscillatory temperature fields, which are depicted in Figure 3 for a blob with $A = 0.1$, $R_b = 10.6$, $Z_b = 0.0$, $\varphi_b = \pi$, $\sigma_R = \sigma_Z = 0.1$, and $\sigma_{\varphi} = 2$. The oscillations arise because the adjoint of the interpolation matrices $I^{\{+, -\}}$ do no longer coincide with the three dimensional weights for all cells. Hence, the transformation is not unitary since $\nabla \cdot \hat{\mathbf{b}} \neq 0$ for the investigated magnetic field. For the aligned FD schemes the position of the the interpolation points is always in the center of the sampling points of the interpolating polynomials. As a consequence the corrugations are better suppressed than for the aligned dG schemes. The initialized structure is not field aligned and bean like temperature fields appear for all aligned schemes, whereas the LDG scheme yields smooth results, which is depicted in Figure 4.

In Figure 5a) and Figure 5b) we show that energy is conserved for all self-adjoint schemes. The direct aligned schemes fail in conserving the L^1 norm. We note here that the self-adjoint schemes are also superior in terms of numerical stability. This is based on the fact that the L^2 norm of the self-adjoint schemes is always $\langle T, DT \rangle \leq 0^2$.

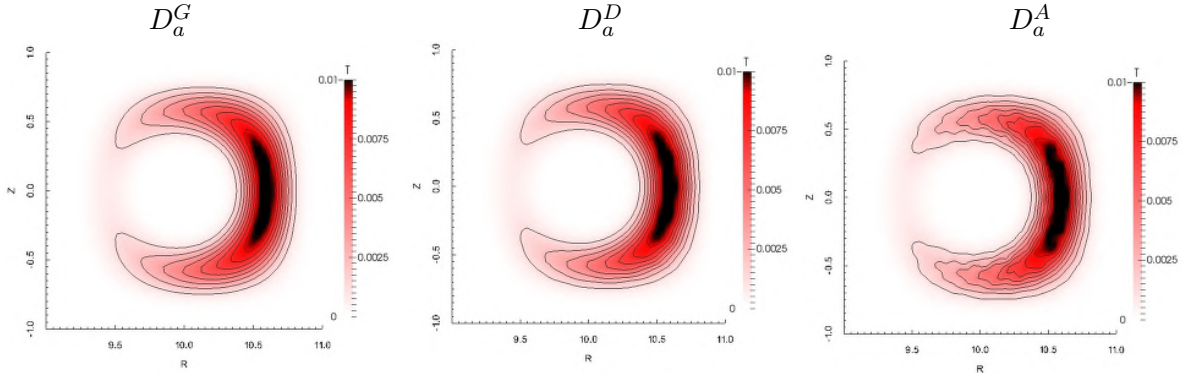


FIG. 3: These contour plots show the evolution of a three dimensional Gaussian blob at $t = 1$ and $\varphi = \pi$ for the non-aligned LDG scheme (left), the direct aligned scheme (center) and the self-adjoint aligned scheme (right). The latter shows up spurious oscillatory temperature fields. The bean like temperature fields of the aligned discretizations are a consequence of the finite resolution in the direction of φ unlike the non-aligned discretization, which has smooth fields even for moderately resolved cases. The resolution was set to $P_{RZ} = 3$, $N_R = N_Z = 20$, $N_\varphi = 21$.

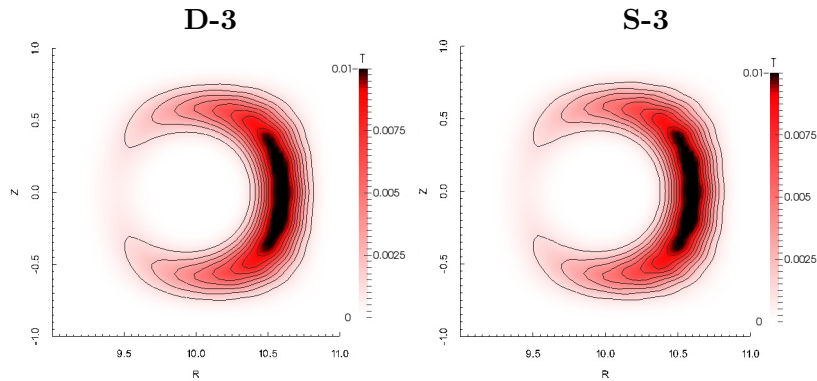


FIG. 4: Result of simulation of Gaussian blob at $t = 1$ and $\varphi = \pi$ for aligned FD schemes. Resolution was set to $N_R = N_Z = 60$, $N_\varphi = 20$.

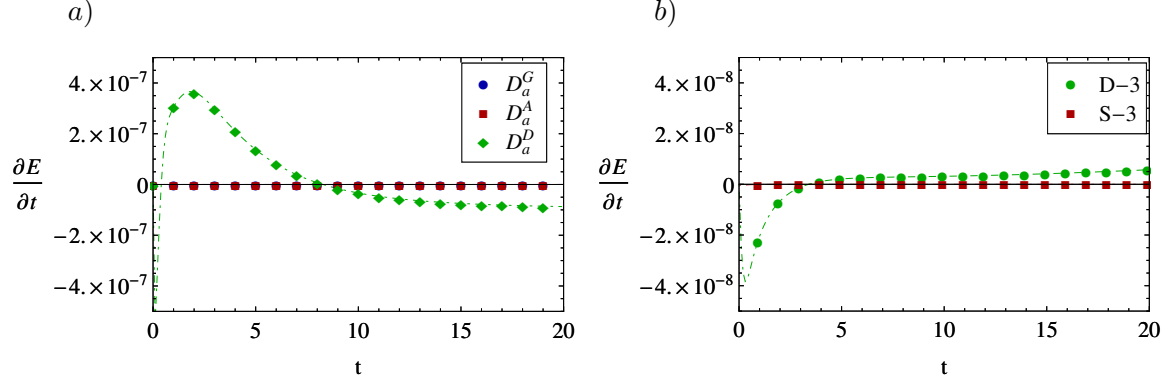


FIG. 5: a) The energy conservation over time for the averaged non-aligned LDG scheme (blue circles), the averaged direct aligned scheme (green rhombi) and the averaged self-adjoint aligned scheme (red squares). The resolution was set to $P_{RZ} = 3$, $N_R = N_Z = 20$, $N_\varphi = 20$. b) The energy conservation over time for the **D-3** scheme (green rhombi) and the **S-3** scheme (red squares). The resolution was set to $N_R = N_Z = 60$, $N_\varphi = 20$

TABLE VI: L^2 error ϵ_{f_1} and orders of accuracy for the averaged non-aligned LDG scheme, the averaged direct aligned scheme and the averaged self-adjoint aligned scheme at $t = 0.01$. The time step is fixed to $\Delta t = 0.0001$.

	D_a^G		D_a^D		D_a^A	
$\Delta\varphi$	L^2 error	order	L^2 error	order	L^2 error	order
$2\pi/6$	2.58E-04	–	7.48E-04	–	7.48E-04	–
$2\pi/18$	3.50E-05	1.82	4.62E-04	0.44	4.64E-04	0.44
$2\pi/54$	3.80E-06	2.02	5.18E-05	1.99	1.15E-04	1.27
$2\pi/162$	–	–	5.32E-06	2.07	4.45E-05	0.86

2. Profile maintenance

We initialize a profile of the form $f_0 = 0.1\psi_p^2$ for which the parallel Laplacian vanishes exactly to zero $\Delta_{\parallel}f_0 = 0$. Hence, the initial state is conserved over time and deviations are a measure for the numerical perpendicular heat flux or numerical sinks and sources. Consequently, we compute the relative error via $\epsilon_{f_0} = \|f_t - f_0\|_{L^2} / \|f_0\|_{L^2}$. In Figure 6a) we analyze

its time evolution for three different perpendicular resolutions $N_R = N_Z = \{5, 20, 80\}$ fixing the resolution in φ to $N_\varphi = 10$ and polynomial coefficients to $P_\varphi = 1$ and $P_{RZ} = 3$. We observe that the aligned dG schemes are superior to the non-aligned LDG scheme for low resolutions. However, for finer resolutions all three schemes do have nearly the same numerical perpendicular heat flux. This error decreases with the order of the interpolating polynomial, which is shown in Table VII at $t = 5$. Here, we observe again superconvergence for the non-aligned LDG scheme. Furthermore, we note that ϵ_{f_0} is independent of N_φ for the non-aligned LDG scheme, whereas it increases with N_φ^2 for the aligned schemes¹. This is reasoned on the aligned differences, which are inversely proportional to N_φ^2 for a $k_{\parallel} = 0$ mode.

For the aligned FD schemes Figure 6b) shows that the **D-3** scheme exhibits a much higher numerical perpendicular heat transport than the **S-3** scheme, also if $\nabla \cdot \hat{\mathbf{b}} \neq 0$.

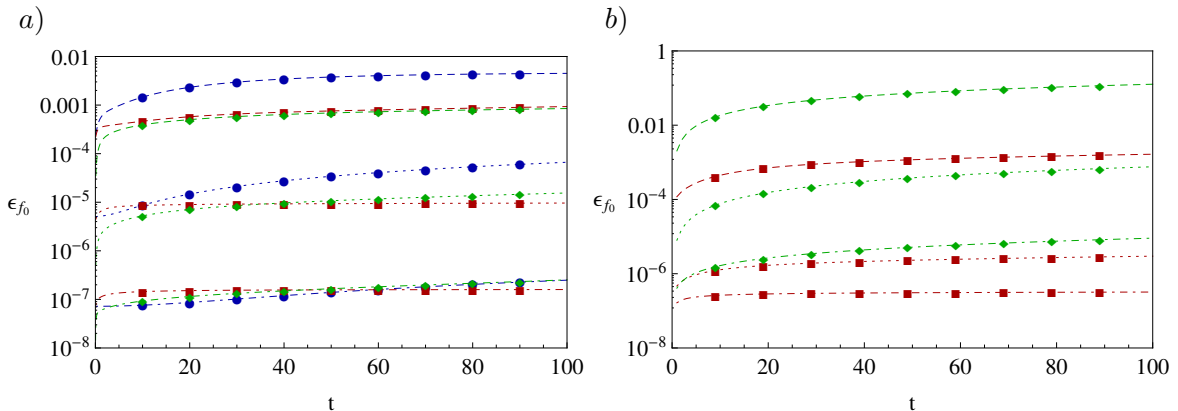


FIG. 6: a) The relative error ϵ_{f_0} over time for the non-aligned LDG scheme (blue circles), the direct aligned scheme (green rhombi) and the self-adjoint aligned scheme (red squares) for three different perpendicular resolutions $N_R = N_Z = \{5, 20, 80\}$ (dashed, dotted, dot-dashed). b) The relative error ϵ_{f_0} over time for the **D-3** scheme (green rhombi) and the **S-3** scheme (red squares) for three different perpendicular resolutions $N_R = N_Z = \{15, 60, 240\}$ (dashed, dotted, dot-dashed).

VI. CONCLUSION

We have presented three different dG discretizations for the parallel diffusion operator. The non-aligned LDG discretization is superior to the two aligned dG schemes, since it is

TABLE VII: L^2 error ϵ_{f_0} and orders of accuracy for the averaged non-aligned LDG scheme, the averaged direct aligned scheme and the averaged self-adjoint aligned scheme

$\Delta R = \Delta Z$	D_a^G		D_a^D		D_a^A	
	L^2 error	order	L^2 error	order	L^2 error	order
2/5	9.74E-04	–	3.05E-04	–	4.04E-04	–
2/10	7.22E-05	3.75	3.11E-05	3.29	6.22E-05	2.70
2/20	6.22E-06	3.54	3.91E-06	2.99	8.13E-06	2.94
2/40	6.44E-07	3.27	4.89E-07	3.00	1.01E-06	3.00
2/80	7.31E-08	3.14	7.75E-08	2.66	1.36E-07	2.90

flexible in the order of convergence whilst keeping the numerical perpendicular heat fluxes at a small level and conserving energy exactly. Our numerical measurements revealed that in general $\nabla \cdot \hat{\mathbf{b}} \neq 0$ cases the aligned dG schemes may exhibit stagnating, reduced or irregular convergence rates whereas the non-aligned LDG scheme remains robust. However, especially for flute modes and coarse resolutions the aligned dG schemes are slightly advantageous to the non-aligned LDG scheme. We compared the latter dG schemes to the aligned FD schemes of References^{1,2} for a magnetic field with $\nabla \cdot \hat{\mathbf{b}} \neq 0$. The direct aligned FD scheme converges with robust rates but is inferior to the self-adjoint aligned FD scheme regarding energy conservation and flute mode maintenance. On the downside the latter scheme showed up degraded and anomalous convergence rates due to the appearance of few corrugations on the grid scale. The herein presented dG discretizations for the parallel diffusion operator are implemented into a **F**ull-F **E**lectromagnetic model in **T**ORoidal geometry (**FELTOR**) and support the computation of long term turbulence simulations of X-point equilibria. Those results are postponed to future publications.

ACKNOWLEDGEMENTS

The authors want to thank Alexander Kendl and Lukas Einkemmer (U Innsbruck) and Hariri F. (EPFL Lausanne) for contributing to this work with fruitful comments. This work was supported by the Austrian Science Fund (FWF) Y398. Matthias Wiesenberger acknowledges further support by a ÖAW KKKÖ Impulsprojekt. This work has been carried out

within the framework of the EUROfusion Consortium and has received funding from the Euratom research and training programme 2014-2018 under grant agreement No 633053. The views and opinions expressed herein do not necessarily reflect those of the European Commission. The computational results presented have been achieved in part using the Vienna Scientific Cluster (VSC). The research leading to these results has partly received funding from the European Research Council under the European Unions Seventh Framework Programme (FP7/2007-2013)/ERC Grant Agreement No. 277870. A part of this work was carried out using the HELIOS supercomputer system at Computational Simulation Centre of International Fusion Energy Research Centre (IFERC-CSC), Aomori, Japan, under the Broader Approach collaboration between Euratom and Japan, implemented by Fusion for Energy and JAEA.

REFERENCES

- ¹A. Stegmeir, D. Coster, O. Maj, and K. Lackner, *Contributions to Plasma Physics* **54**, 549 (2014).
- ²A. Stegmeir, D. Coster, O. Maj, K. Hallatschek, and K. Lackner, arXiv:1505.02040 [physics.plasm-ph], Submitted to *Computer Physics Communications*.
- ³W. D’haeseleer, W. Hitchon, J. Callen, and J. Shohet, *Flux Coordinates and Magnetic Field Structure*, Springer Series in Computational Physics (Springer, 1991).
- ⁴B. D. Scott, *Physics of Plasmas* **8**, 447 (2001).
- ⁵T. T. Ribeiro and B. D. Scott, *IEEE Transactions on Plasma Science* **38** (2010).
- ⁶I. Babuška and M. Suri, *SIAM Journal on Numerical Analysis* **29**, 1261 (1992).
- ⁷S. Günter, Q. Yu, J. Krüger, and K. Lackner, *Journal of Computational Physics* **209**, 354 (2005).
- ⁸C. Sovinec, A. Glasser, T. Gianakon, D. Barnes, R. Nebel, S. Kruger, D. Schnack, S. Plimpton, A. Tarditi, M. Chu, and the NIMROD Team, *Journal of Computational Physics* **195**, 355 (2004).
- ⁹S. Günter, K. Lackner, and C. Tichmann, *Journal of Computational Physics* **226**, 2306 (2007).
- ¹⁰M. Shashkov and S. Steinberg, *Journal of Computational Physics* **118**, 131 (1995).
- ¹¹B. Cockburn and C. W. Shu, *SIAM Journal on Numerical Analysis* **35**, 2440 (1998).

- ¹²F. Hariri and M. Ottaviani, *Computer Physics Communications* **184**, 2419 (2013).
- ¹³B. van Es, B. Koren, and H. J. De Blank, *Journal of Computational Physics* , 526 (2014).
- ¹⁴F. Hariri, P. Hill, M. Ottaviani, and Y. Sarazin, *Physics of Plasmas* **21**, 082509 (2014).
- ¹⁵A. Stegmeir, *GRILLIX: A 3D turbulence code for magnetic fusion devices based on a field line map*, Ph.D. thesis, Technische Universität München (2015), iPP Report 1/356.
- ¹⁶P. Sharma and G. W. Hammett, *Journal of Computational Physics* **227**, 132 (2007).
- ¹⁷L. Einkemmer and M. Wiesenberger, *Compututer Physics Communications* **185**, 2865 (2014).
- ¹⁸M. Abramowitz and I. Stegun, *Handbook of mathematical functions*, 10th ed. (Dover Publishing Inc. New York, 1972).
- ¹⁹B. Cockburn, G. Kanschat, I. Perugia, and D. Schotzau, *SIAM Journal on Numerical Analysis* **39**, 264 (2001).
- ²⁰T. Frankel, *The geometry of physics*, 2nd ed. (Cambridge University Press, 2004).
- ²¹J. J. Yoh and X. L. Zhong, *AIAA Journal* **42**, 1593 (2004).